Deformation of a helical filament by flow and electric or magnetic fields

MunJu Kim* and Thomas R. Powers†
Division of Engineering, Brown University, Providence, Rhode Island 02912, USA
(Received 25 August 2004; published 28 February 2005)

Motivated by recent advances in the real-time imaging of fluorescent flagellar filaments in living bacteria [Turner, Ryu, and Berg, J. Bacteriol. **82**, 2793 (2000)], we compute the deformation of a helical elastic filament due to flow and external magnetic or high-frequency electric fields. Two cases of deformation due to hydrodynamic drag are considered: the compression of a filament rotated by a stationary motor and the extension of a stationary filament due to flow along the helical axis. We use Kirchhoff rod theory for the filament, and work to linear order in the deflection. Hydrodynamic forces are described first by resistive-force theory, and then for comparison by the more accurate slender-body theory. For helices with a short pitch, the deflection in axial flow predicted by slender-body theory is significantly smaller than that computed with resistive-force theory. Therefore, our estimate of the bending stiffness of a flagellar filament is smaller than that of previous workers. In our calculation of the deformation of a polarizable helix in an external field, we show that the problem is equivalent to the classical case of a helix deformed by forces applied only at the ends.

DOI: 10.1103/PhysRevE.71.021914 PACS number(s): 87.16.Qp, 46.70.Hg, 47.15.Gf, 82.37.Rs

I. INTRODUCTION

Many micro-organisms swim using thin, flexible flagella. For example, a mammalian sperm cell swims by sending traveling waves of bending down its flagellum [1]. At these micron length scales, the inertia of both the cell and the fluid is unimportant and viscous effects dominate: the Reynolds number is very low. At zero Reynolds number, reciprocal motions like the waving of a rigid oar generate zero net translation per period [2]. Thus, the flexibility of the sperm flagellum is crucial for motion. Another example where the flexibility of the flagellum is important is the chemotaxis of the bacterium *Escherichia coli* [3]. These cells use several rotating helical flagella to swim. Each flagellum must be stiff enough to hold its helical shape when subject to viscous stresses; if the flagellar filaments were too flexible, they would twist and bend as they rotate and fail to generate propulsive force. On the other hand, if the filaments were too stiff, then it would be impossible to form the bundle which pushes the cell along [4], since the filaments in a rotating bundle must continuously deform [5]. Furthermore, the filaments must be sufficiently flexible that viscous stresses can trigger the polymorphic transition which the cell uses to change its swimming direction [4,6].

Despite the importance of the interplay of flexibility and hydrodynamics, most theoretical treatments of the dynamics of flagella do not fully incorporate the elastic response of the filament with the long-range hydrodynamic interactions of low-Reynolds-number flow. For example, many workers have solved for the flows generated by a prescribed motion of thin filaments, such as the planar traveling bending waves of sperm flagella [7], or the rotation of one or more rigid helices [8–10]. These approaches disregard the elasticity of the filament, but use slender-body theory [7,11] or related techniques [12] to accurately capture the hydrodynamic interactions. A common alternative approach is to use Kirchhoff rod theory (or some generalization) to model the elastic nature of the filament, but to approximate the hydrodynamic forces using resistive-force theory [13–19]. In resistive-force theory [20], the force on a short segment of the filament is proportional to the velocity of the segment, but the motion of the fluid is otherwise ignored. Finally, there have been far fewer analyses of flagellar motion that accurately treat both the elastic and viscous parts of the problem. One of the earliest is a comparison between resistive-force theory and slender-body theory for a model of the active bending moments for a sperm flagellum [21]. These authors found that resistive-force theory (with suitably adjusted resistance coefficients) is accurate for a waving filament without a cell body, but that slender-body theory is necessary for good accuracy when the cell body is included. Recently, the bundling of flexible bacterial flagella has been numerically simulated using the method of regularized Stokeslets [22].

In this article, we combine slender-body theory with Kirchhoff rod theory to study a simple illustrative problem, the deflection of a helical filament by flow. The combination of slender-body theory (rather than resistive-force theory) with elasticity theory is an improvement over previous work. Since we consider small deflections (too small to trigger polymorphic transformations), we work to first order in the deformation. The small expansion parameter depends on the problem. For example, for loading by hydrodynamic drag, we expand in $\eta v R^2 L/A$, where η is the viscosity, v is the fluid velocity, R is the helical radius, L is the contour length of the helix, and A is the bending stiffness [see Eqs. (25) and (11) below]. For characteristic orders of magnitude of $\eta = 10^{-3}$ N s/m^2, $v = 10$ μm/s, $R = 0.5$ μm, $L = 10$ μm, and $A = 10^{-24}$ N m^2, $\eta v R^2 L/A$ is a fraction of a percent, justifying our approximation. Thus, to leading order in the small parameter, the flow is that generated by the undeformed helix, but the deformation depends on the flow. In addition to al-

*Electronic address: mjkim@math.utah.edu; present address: Department of Mathematics, University of Utah, Salt Lake City, UT 84112, USA.
†Electronic address: Thomas_Powers@brown.edu

lowing a quantitative assessment of the accuracy of resistive-force theory as the helix shape varies from close- to open-coiled (small to large pitch), our calculation can be used to determine the stiffness of the bacterial flagellar filament.

Measurements of filament elasticity vary over a wide range. Fujime, Maruyama, and Asakura used light scattering to find a bending stiffness $A \approx (2-4)\times 10^{-24}$ N m^2 for *Salmonella typhimurium* filaments [23]. Later, Hoshikawa and Kamiya measured the extension of an *S. typhimurium* filament subject to flow along the helix axis to find a shear modulus of 10^{10} N/m^2 [24]. For a rod with radius $a = 10$ nm, this shear modulus corresponds to a twist modulus $C \approx 10^{-22}$ N m^2 [25]. Using electron micrographs of isolated filaments, Trachtenberg and Hammel reported Young's moduli ranging from $E \approx 1.04\times 10^{10}$ N/m^2 to $E \approx 1.77 \times 10^{11}$ N/m^2 for a variety of filament types. For a radius $a \approx 10$ nm, these values correspond to a range of bending stiffnesses from $A \approx 8\times 10^{-23}$ N m^2 to $A \approx 1\times 10^{-21}$ N m^2 [26]. More recently, Takano and co-workers estimated $A \approx 10^{-24}$ N m^2 for *Vibrio alginolyticus* by examining the deformation of the filament of a swimming bacterium [19]. Motivated by these discrepancies, and by recent advances in fluorescent labeling of the filament of *E. coli* [6], we revisit the calculation of the extension of a filament due to axial flow. Our calculation differs from that of Hoshikawa and Kamiya, since we use Kirchhoff rod theory instead of modeling the filament as a sequence of beads, and since we use slender-body hydrodynamics instead of resistive-force theory. We show that resistive-force theory is highly inaccurate for the close-coiled flagella studied by Hoshikawa and Kamiya. Applying the results of the slender-body theory calculation to the data of [24], and assuming $C=A$, we estimate $A \approx 3\times 10^{-24}$ N m^2.

We also present a calculation of the compression of a rotating flexible helix. This calculation is closely related to the calculations of Takano and co-workers [18,19], with two important differences: (i) our calculation is valid for a helix rotated by a stationary motor, whereas Takano *et al.* include the effect of translation due to swimming, and (ii) we incorporate hydrodynamic interactions in our slender-body theory computation. We show that for an open-coiled helix, resistive-force theory gives a modest error for the force per unit length. Therefore, our calculations lend further support to those of Takano *et al.* Since our calculations neglect the disturbance of the flow due to nearby walls or the cell body, our estimate of the bending stiffness is still only accurate within an order of magnitude. The purpose of these calculations is to describe our method in a simplified setting.

Since biological filaments are often polarizable by electric [27] or magnetic [28] fields, we also study the deformation of a filament in an external field. In the case of an electric field, we assume the filament is uncharged, or, if charged, subject to a rapidly oscillating ac electric field. Thus, unlike viscous drag, which amounts to distributed loading by an external force per unit length, the induced polarization leads to distributed loading by an external *moment* per unit length. We show that to first order in the deflection (the small expansion parameter in this case is $\chi_a R^2 E^2/A$, where χ_a is the anisotropy in the susceptibility per length and E is the electric field), the moment balance equations for the external field problem are equivalent to the equations for a helix in no field but subject to end-loading by forces only. Although we focus on bacterial flagella, our calculations are applicable to the deflection of any flexible helical filament.

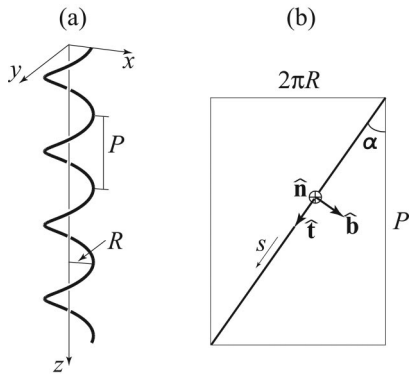

FIG. 1. (a) A helix with pitch P and radius R. (b) One turn of a helix "unrolled," showing the pitch angle α, and the orientation of the Serret-Frenet frame $\{\hat{\mathbf{t}},\hat{\mathbf{n}},\hat{\mathbf{b}}\}$.

The first section of the body of this article describes the model. We review the geometry of a helix and introduce the material frame. Then we describe the constitutive relations for a helical filament, resistive-force theory, and slender-body hydrodynamics. This section closes with the formulation of the equations for a thin polarizable filament in an external field. The next section presents the results. We give explicit formulas for the deflection of a helix in axial and rotational flow using resistive-force theory for a helix with many turns. Then we compute the deflection for an open-coiled and a close-coiled helix using slender-body theory, and compare with resistive-force theory. In the last part of this section, we present the results of the calculation of a polarizable helix in a field. The final section discusses the application of our results to experiments and offers some conclusions. The Appendix describes the details of the calculations of the deformations.

II. MODEL

A. Geometry

Consider a helix of radius R and pitch P, with its axis aligned along the z axis (see Fig. 1),

$$\mathbf{r}(z) = (R\cos(2\pi z/P), R\sin(2\pi z/P), z). \tag{1}$$

For fixed contour length L, the shape of the helix is completely specified by R/L and the pitch angle α, where $\tan\alpha = 2\pi R/P$. (Note that the pitch angle changes sign under reflection.) Equivalently, the helix is specified by its curvature κ and torsion τ, which are defined by the rates of change of the Serret-Frenet frame [29],

$$\frac{\partial}{\partial s}\begin{pmatrix}\hat{\mathbf{n}}\\ \hat{\mathbf{b}}\\ \hat{\mathbf{t}}\end{pmatrix} = \begin{pmatrix}0 & \tau & -\kappa\\ -\tau & 0 & 0\\ \kappa & 0 & 0\end{pmatrix}\begin{pmatrix}\hat{\mathbf{n}}\\ \hat{\mathbf{b}}\\ \hat{\mathbf{t}}\end{pmatrix}, \tag{2}$$

where $s = z\sqrt{1+4\pi^2R^2/P^2}$ is arc length, $\hat{\mathbf{t}} \equiv \partial\mathbf{r}/\partial s$ is the tangent, $\hat{\mathbf{n}}$ is the normal, and $\hat{\mathbf{b}} = \hat{\mathbf{t}}\times\hat{\mathbf{n}}$ is the binormal. Inspec-

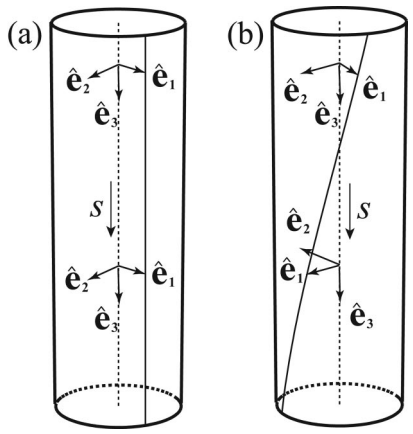

FIG. 2. (a) The material frame for a straight and untwisted rod. (b) The material frame for a straight rod with right-handed (positive) twist; $\hat{\mathbf{e}}_1$ and $\hat{\mathbf{e}}_2$ rotate about $\hat{\mathbf{e}}_3$ as s increases.

tion of Fig. 1(b) reveals that $\hat{\mathbf{t}}=\cos\alpha\hat{\mathbf{z}}+\sin\alpha\hat{\boldsymbol{\varphi}}$, and thus $\hat{\mathbf{n}}=-\hat{\boldsymbol{\rho}}$ and $\hat{\mathbf{b}}=-\cos\alpha\hat{\boldsymbol{\varphi}}+\sin\alpha\hat{\mathbf{z}}$, where $\varphi\equiv 2\pi z/|P|$ and ρ are cylindrical polar coordinates. These formulas with Eq. (2) imply that a helix has curvature $\kappa_0=\sin^2\alpha/R$ and torsion $\tau_0=\cos\alpha\sin\alpha/R$, where the subscripts denote the absence of external stress.

B. Material frame

Now consider an elastic rod. In addition to the curvature and torsion of the rod centerline, there is a new degree of freedom, the twist (for simplicity we forbid stretching of the centerline and relative shear between nearby cross sections). To describe these degrees of freedom, define a right-handed orthonormal material frame $\{\hat{\mathbf{e}}_1,\hat{\mathbf{e}}_2,\hat{\mathbf{e}}_3\}$ such that $\hat{\mathbf{e}}_1$ and $\hat{\mathbf{e}}_2$ align along the principal axes of the rod cross section, and $\hat{\mathbf{e}}_3=\hat{\mathbf{t}}$ [25]. Since this frame is a *material* frame, the frame rotates with the material as the rod bends and twists—we can think of the vectors as being embedded in the material. The twist Ω_3 is the rate at which $\hat{\mathbf{e}}_1$ rotates about $\hat{\mathbf{e}}_3$ as s increases, and the two components of curvature of the rod centerline, Ω_1 and Ω_2, are the rates at which $\hat{\mathbf{e}}_3$ rotates about $\hat{\mathbf{e}}_1$ and $\hat{\mathbf{e}}_2$, respectively, as s increases (see Fig. 2). The local angular velocity $\boldsymbol{\omega}$ of the frame at a given s is defined in a similar way; thus

$$\frac{\partial\hat{\mathbf{e}}_i}{\partial s}=\boldsymbol{\Omega}\times\hat{\mathbf{e}}_i, \tag{3}$$

$$\frac{\partial\hat{\mathbf{e}}_i}{\partial t}=\boldsymbol{\omega}\times\hat{\mathbf{e}}_i. \tag{4}$$

The vector $\boldsymbol{\Omega}=\Omega_1\hat{\mathbf{e}}_1+\Omega_2\hat{\mathbf{e}}_2+\Omega_3\hat{\mathbf{e}}_3$ is related to the instantaneous strain in the rod.

Note that if the cross section is circular, then there are many equivalent choices for the direction of $\hat{\mathbf{e}}_1$. Assuming a circular cross section for the naturally helical rod, we choose $\{\hat{\mathbf{e}}_1,\hat{\mathbf{e}}_2\}$ to align with $\{\hat{\mathbf{n}},\hat{\mathbf{b}}\}$ in the absence of external forces and moments. (For small perturbations to a helix, the Serret-Frenet frame is always well-defined; see [30–32] for discussions of the *natural frame* which is well-defined even at points where $\kappa=0$.) When forces and moments are applied to the filament, both the Serret-Frenet frame and the material frame at each point rotate, but not necessarily by the same amount. Given $\boldsymbol{\Omega}$, the material frame is determined by integrating Eq. (3). Integration of $\hat{\mathbf{e}}_3$ yields the shape $\mathbf{r}(s)$. The details of these integrations (for small deflection) are described in the Appendix.

C. Constitutive relations

The rate of rotation $\boldsymbol{\Omega}$ of the material frame defines the shape of an elastic rod. Let $\boldsymbol{\Omega}^{(0)}$ denote the rate of rotation in the absence of external forces and moments. Then the linear constitutive relation,

$$\mathbf{M}=A(\Omega_1-\Omega_1^{(0)})\hat{\mathbf{e}}_1+B(\Omega_2-\Omega_2^{(0)})\hat{\mathbf{e}}_2+C(\Omega_3-\Omega_3^{(0)})\hat{\mathbf{e}}_3, \tag{5}$$

determines the moment $\mathbf{M}$ of elastic stresses acting on a cross section with outward normal $\hat{\mathbf{e}}_3$ at s [25]. Since we consider helices with circular cross sections, $A=B$. Comparison of Eq. (2) and Eq. (3) when the filament is undeformed shows that $\Omega_1^{(0)}=0$, $\Omega_2^{(0)}=\kappa_0$, and $\Omega_3^{(0)}=\tau_0$. Thus,

$$\mathbf{M}=A[\Omega_1\hat{\mathbf{e}}_1+(\Omega_2-\kappa_0)\hat{\mathbf{e}}_2]+C(\Omega_3-\tau_0)\hat{\mathbf{e}}_3. \tag{6}$$

We make one final simplification of the constitutive relations by setting $C=A$. For a rod made from an isotropic linearly elastic material, $C/A=2\mu/E=1/(1+\nu)$, where μ is the shear modulus, E is the Young's modulus, and ν is the Poisson ratio [25]. For an ordinary material, $0\leqslant\nu\leqslant 1/2$; therefore, C/A lies in the narrow range between $2/3$ and 1.

The internal elastic stresses exert a force $\mathbf{F}$ as well as a moment $\mathbf{M}$ on the cross section at s. Balancing the forces and moments on an element of the rod of length ds leads to

$$\frac{\partial\mathbf{F}}{\partial s}+\mathbf{K}=\mathbf{0}, \tag{7}$$

$$\frac{\partial\mathbf{M}}{\partial s}+\hat{\mathbf{t}}\times\mathbf{F}+\mathbf{N}=\mathbf{0}, \tag{8}$$

where $\mathbf{K}$ is the external force per unit length and $\mathbf{N}$ is the external torque per unit length [25].

D. Hydrodynamic drag

For a flagellum, the external forces and moments arise from hydrodynamic drag. In this article, we will compare resistive-force theory and slender-body theory. In resistive-force theory [20], the drag force per unit length is proportional to the local rod velocity $\mathbf{v}$ relative to the fluid velocity far from the rod,

$$\mathbf{K}=-\zeta_\perp[\mathbf{v}-(\hat{\mathbf{t}}\cdot\mathbf{v})\hat{\mathbf{t}}]-\zeta_\parallel(\hat{\mathbf{t}}\cdot\mathbf{v})\hat{\mathbf{t}}. \tag{9}$$

This expression asymptotically approaches the exact relation as the radius a becomes much smaller than the rod's length or typical radius of curvature λ [33]. In this limit, the resistance coefficients take the form

$$\zeta_\perp \sim 4\pi\eta/\ln(\lambda/a), \tag{10}$$

$$\zeta_\parallel \sim 2\pi\eta/\ln(\lambda/a), \tag{11}$$

where η is viscosity and a is the filament diameter. The force per unit length is anisotropic, with the resistance to motion tangential to the rod half the resistance of motion perpendicular to the rod. Note that replacing λ by 2λ in Eqs. (10) and (11) merely leads to subdominant additive terms in the denominator. Since the ratio $a/\lambda \approx 10^{-3}$ for a real flagellum, the asymptotic limit of Eqs. (10) and (11), in which $\ln(\lambda/a) \gg 1$, is not attained in practice. Therefore, various authors have proposed different values for the resistance coefficients $\zeta_\parallel$ and $\zeta_\perp$, depending on the shape of the flagellum and its motion [7,11,20,34]. Nevertheless, since we are only using resistive-force theory to build intuition and to compare with slender-body theory, we will use Eqs. (10) and (11) with $\lambda = R/\sin(\alpha)$, the periodicity of the helix measured along the arc length.

The viscous moment per unit length resisting the rotation of an element of the rod about $\hat{\mathbf{t}}$ is

$$\mathbf{N} = -\zeta_r(\hat{\mathbf{t}} \cdot \boldsymbol{\omega})\hat{\mathbf{t}}, \tag{12}$$

where $\zeta_r = 4\pi\eta a^2$ is the rotational drag coefficient. This moment may be safely neglected for a helix of radius $R \gg a$, since the contributions to moment balance, Eq. (8), from $\mathbf{N}$ are smaller than the leading contributions from the translation of rod elements by a factor of $(a/R)^2$.

Resistive-force theory is simple to use, but as we will see, it is not always accurate. Furthermore, resistive-force theory makes no prediction for the disturbance flow induced by a moving flagellum. Slender-body theory overcomes both of these defects. In slender-body theory, the flow induced by a moving flagellum is approximated by the flow induced by a line of singular solutions to the Stokes equations (the equations of flow at zero Reynolds number) for the fluid velocity $\mathbf{u}$,

$$\eta\nabla^2\mathbf{u} - \nabla p = \mathbf{0}, \tag{13}$$

$$\nabla \cdot \mathbf{u} = 0. \tag{14}$$

One of the singular solutions is the Stokeslet, $u_i(\mathbf{x}) = S_{ij}(\mathbf{x} - \mathbf{x}')f_j$, which is the flow at $\mathbf{x}$ generated by a point force $\mathbf{f}$ at $\mathbf{x}'$. To determine the Stokeslet tensor S_{ij}, we solve the Stokes equations (13) and (14) with a point force,

$$\eta\nabla^2(S_{ij}f_j) - \nabla_i p + f_i\delta(\mathbf{x} - \mathbf{x}') = 0 \tag{15}$$

$$\frac{\partial}{\partial x_i}S_{ij} = 0, \tag{16}$$

to find

$$S_{ij}(\mathbf{y}) = \frac{\delta_{ij}}{|\mathbf{y}|} + \frac{\mathbf{y}_i\mathbf{y}_j}{|\mathbf{y}|^3}, \tag{17}$$

with $\mathbf{y} \equiv \mathbf{x} - \mathbf{x}'$ [7,11]. The other singular solution is the doublet $u_i(\mathbf{x}) = D_{ij}(\mathbf{x} - \mathbf{x}')g_j$, which is the flow at $\mathbf{x}$ induced by a dipole source of strength $\mathbf{g}$ at $\mathbf{x}'$. The doublet tensor is

$$D_{ij} = \frac{\delta_{ij}}{|\mathbf{y}|^3} + \frac{3\mathbf{y}_i\mathbf{y}_j}{|\mathbf{y}|^5}, \tag{18}$$

again with $\mathbf{y} \equiv \mathbf{x} - \mathbf{x}'$. Just as in resistive-force theory, the contribution to the flow from the rotation of each segment of the filament about its tangent vector is subleading. Since the Stokes equations are linear, the flow is given by a superposition of these solutions, weighted by the force per unit length $-\mathbf{K}(s)$ of the flagellum on the fluid [7],

$$\mathbf{u}_i(\mathbf{x}) = -\sum_j \int ds \left[\frac{S_{ij}K_j}{8\pi\eta} - \frac{a^2 D_{ij}K_{\perp j}}{16\pi\eta} \right]. \tag{19}$$

In Eq. (19), $\mathbf{K}_\perp = \mathbf{K} - (\hat{\mathbf{t}} \cdot \mathbf{K})\hat{\mathbf{t}}$, S_{ij} and D_{ij} are evaluated at $\mathbf{x} - \mathbf{r}(s)$, and $\mathbf{r}(s)$ is the flagellum centerline.

Since the helix is flexible, there will be a disturbance flow of $O(\eta v R^2 L/A)$ due to the deformation of the filament. However, the leading-order flow is $O(1)$. Therefore, to calculate the deformation of the filament to first order in $\eta v R^2 L/A$, we only need to consider the flow generated by a rigid helix. Furthermore, only the force per unit length $\mathbf{K}$, and not the flow $\mathbf{u}$, is required to compute the deformation. Our calculations are similar to but simpler than those of our previous work [10], where we studied the forces and flows generated by two rotating rigid helices.

To solve for force per unit length, we discretize Eq. (19), approximating the filament with a series of short straight segments [10]. We work in the frame for which the fluid velocity vanishes far from the filament; thus, the velocity of the filament is $\mathbf{v} = v\hat{\mathbf{z}}$ for the case of translation and $\mathbf{v} = \omega\hat{\mathbf{z}} \times \mathbf{r}(s)$ for the case of rotation. Note that there are no fictitious forces in the rotating frame at zero Reynolds number. Given the velocity at the filament, we enforce the no-slip boundary condition at a point just at the surface in the middle of each straight segment, $\mathbf{x}_\alpha = \mathbf{r}(s_\alpha) + a\hat{\mathbf{n}}(s_\alpha)$, where α labels the segments and $\hat{\mathbf{n}}(s)$ is the unit normal vector at s. The nonzero filament radius a prevents the singular solutions from diverging. Combining the no-slip condition with the discretized form of Eq. (19) yields a set of linear equations for the force per unit length,

$$v_{i\alpha} = \sum_{j\beta} Q_{i\alpha,j\beta}K_{j\beta}, \tag{20}$$

where $v_{i\alpha}$ is the velocity at $\mathbf{x}_\alpha$ and $K_{j\beta} = K_j(s_\beta)$. The matrix Q is found by integrating the Stokeslet and doublet solutions along over the segments; explicit formulas for Q are given by Higdon in [7].

E. Polarizable filaments

In this subsection we use the notation of electric polarizability, but the formulas apply equally well to the case of magnetic polarizability. For simplicity, we assume the optical axis of the filament aligns with the tangent vector $\hat{\mathbf{t}}$. The induced polarization per unit length then has the form

$$\mathbf{p} = \chi_\perp[\mathbf{E} - (\hat{\mathbf{t}} \cdot \mathbf{E})\hat{\mathbf{t}}] + \chi_\parallel(\hat{\mathbf{t}} \cdot \mathbf{E})\hat{\mathbf{t}}, \tag{21}$$

where $\chi_\perp$ is the susceptibility for polarization normal to $\hat{\mathbf{t}}$, $\chi_\parallel$ is the susceptibility for polarization along $\hat{\mathbf{t}}$, and $\mathbf{E}$ is the

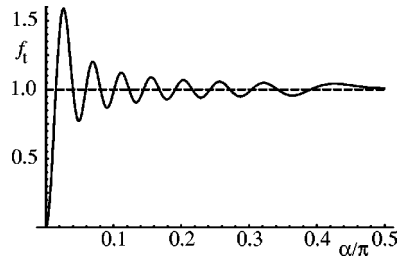

FIG. 3. Dimensionless extension f_t vs pitch angle α for a helix with four turns, $R=0.22$ μm, and $P=2.4$ μm, subject to axial flow. The hydrodynamic forces are calculated using resistive-force theory. The solid line is calculated using the exact expression for f_t, and the dotted line is $f_t=1$, the approximate dimensionless extension to leading order in R/L.

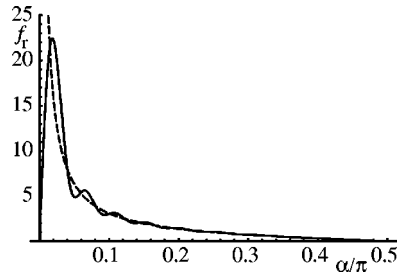

FIG. 4. Dimensionless extension f_r vs pitch angle α for a helix with four turns, $R=0.22$ μm, and $P=2.4$ μm, subject to rotational flow. The solid line is calculated using the exact expression for f_r, and the dotted line is $f_r=\cot\alpha$, the approximate dimensionless extension to leading order in R/L.

external electric field. Thus, the torque per unit length acting on the filament is

$$\mathbf{N}=\mathbf{p}\times\mathbf{E}=\chi_a(\hat{\mathbf{t}}\cdot\mathbf{E})(\hat{\mathbf{t}}\times\mathbf{E}), \tag{22}$$

where $\chi_a\equiv\chi_\parallel-\chi_\perp$ is the anisotropy in the susceptibility per unit length.

III. RESULTS

Before stating our results for the deformation of a helix under distributed loading, it is useful to recall how a helical spring deforms when subject to end loading. The deformation depends strongly on how the ends of the spring are held. We will suppose that one end of the spring, $s=0$, is clamped with $\mathbf{r}(0)=\mathbf{0}$ and $\partial\mathbf{r}/\partial s(0)=\cos\alpha\hat{\mathbf{z}}+\sin\alpha\hat{\boldsymbol{\varphi}}$. [Hinged boundary conditions, such as $\mathbf{M}\cdot\hat{\mathbf{n}}=0$ at $s=0$, are not considered since they would allow the helical axis to rotate about $\hat{\mathbf{n}}(0)$, leading to large displacements.] A common choice for the other end, $s=L$, is to have the line of action of the force $\mathbf{F}=F\hat{\mathbf{z}}$ coincide with the helical axis $\hat{\mathbf{z}}$. This condition leads to a moment $\mathbf{M}=RF\hat{\boldsymbol{\varphi}}$ at $s=L$, where the origin for the moment is $\mathbf{0}$. For $C=A$, the extension of the helix to first order in the dimensionless force FR^2/A is

$$\frac{\delta z_1(L)}{L}=\frac{FR^2}{A}\left\{1-\frac{R}{L}\frac{\sin[(L/R)\sin\alpha]}{\sin\alpha}\right\}. \tag{23}$$

Note that Eq. (23) exhibits the proper limit as $\alpha\to0$ for fixed R. In this limit, the undeformed rod is parallel to the z axis. Since the rod is inextensible, the force does not lead to an increase in the contour length. Since there is still a moment acting at $s=L$, the rod deflects; however, the component of this deflection in the z direction is second order in the dimensionless force, and $\delta z_1(L)=0$. Note also the oscillations in $\delta z_1(L)$ (for fixed L and as a function of α, say) arising from the second term on the right-hand side of Eq. (23). These oscillations become negligible when $R/L\ll1$, indicating that they are an artifact of the boundary conditions. For large L/R, we recover the familiar result (for $C=A$) $\delta z_1(L)=FR^2/A$ [35].

Since $\mathbf{M}(L)=\mathbf{0}$ in all of our distributed loading problems, it is more appropriate to make comparisons with an end-loading problem in which the line of action of the force $\mathbf{F}=F\hat{\mathbf{z}}$ passes through the origin, so that $\mathbf{M}(L)=\mathbf{0}$. The deflection in this case is twice as large,

$$\frac{\delta z_2(L)}{L}=2\frac{FR^2}{A}\left\{1-\frac{R}{L}\frac{\sin[(L/R)\sin\alpha]}{\sin\alpha}\right\}. \tag{24}$$

To see how Eqs. (23) and (24) are derived, see the Appendix.

For distributing loading by viscous drag, the total force on the filament increases with contour length: $F\propto\eta vL$, where v is the characteristic flow velocity. Therefore, using the asymptotic form of the resistive-force coefficients of Eqs. (10) and (11) for simplicity, dimensional analysis implies that the extension of a helix in axial flow obeys

$$\frac{\delta z_t(L)}{L}=\frac{\zeta_\parallel vR^2L}{A}f_t(\alpha,R/L), \tag{25}$$

and the extension of a helix rotating with angular speed ω in a viscous fluid obeys

$$\frac{\delta z_r(L)}{L}=\frac{\zeta_\parallel\omega R^3L}{A}f_r(\alpha,R/L), \tag{26}$$

where f_t and f_r are dimensionless functions, the "t" subscript stands for "translation," and the "r" subscript stands for "rotation." In the Appendix, we also calculate the extension of a helix hanging under its own weight.

For distributed loading of a polarizable filament by an external field $\mathbf{E}=E\hat{\mathbf{z}}$, the moment per unit length is aligned with $\hat{\boldsymbol{\rho}}$, and has no $\hat{\mathbf{z}}$ component [see Eq. (22)]. Integrating $d\mathbf{M}/ds+\mathbf{N}=0$ therefore leads to a total moment that scales with R, not L: $M\propto\chi_aE^2R$. Therefore, the extension obeys

$$\frac{\delta z_f(L)}{L}=\frac{\chi_aE^2R}{A}f_f(\alpha,R/L), \tag{27}$$

where the "f" subscript stands for field. To summarize, we have shown that for a rod in a flow, the extension δz is proportional to L^2; for a rod polarized by an external field, the extension δz is proportional to L.

A. Resistive-force theory

The Appendix gives the details of the calculation of f_t, f_r, and f_f. First we discuss the calculation of extension by drag using the resistive-force theory approximation. The calcula-

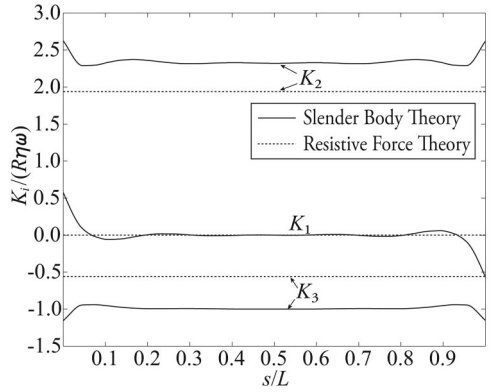

FIG. 5. The viscous drag force per unit length **K**, in units of $R\eta\omega$, for an open-coiled helix rotating with speed ω vs arc length s in units of L. The filament radius is $a=0.01$ μm, the helix radius is $R=0.22$ μm, the pitch is $P=2.4$ μm, and the total arc length is $L \approx 11$ μm.

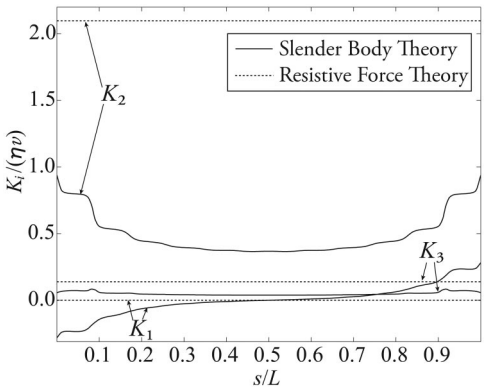

FIG. 6. The viscous drag force per unit length **K**, in units of ηv, for a close-coiled helix subject to axial flow with speed v vs arc length s in units of L. The helix parameters are taken from [24]: the filament radius is $a=0.01$ μm, the helix radius is 0.6 μm, the pitch is 0.5 μm, and the total number of turns is 11.5.

tion can be carried out analytically, but the full expression is too lengthy to give here. Since $L/R \approx 50$ for a normal *E. coli* filament [$R=0.22$ μm, $P=2.4$ μm [6], Fig. 5(a)] with four turns, the leading terms of f_t and f_r in an expansion in R/L give a very good approximation. For a helix immersed in a uniform flow in the positive z direction, we find

$$\frac{\delta z_t(L)}{L} = \frac{\zeta_\parallel v R^2 L}{A}[1 + O(R/L)]. \tag{28}$$

For a helix rotating with angular velocity $\boldsymbol{\omega}=\omega\hat{\mathbf{z}}$,

$$\frac{\delta z_r(L)}{L} = \frac{\zeta_\parallel \omega R^3 L \cot\alpha}{A}[1 + O(R/L)]. \tag{29}$$

When $C=A$, the extension of a helix due to axial flow, Eq. (28), is independent of the pitch angle α, just as in the case of end-loading, Eq. (23). In particular, the sign of the extension is independent of the handedness of the helix. On the other hand, the sign of the extension of a rotating helix depends on the handedness: a left-handed helix ($\alpha<0$) rotating counterclockwise when viewed from the end $s=L$ ($\omega>0$) will compress [$\delta z_r(L)<0$]. Note that the effect of neglecting the subleading terms in R/L is to ignore the effects of boundary conditions. Equations (28) and (29) cannot be correct for all α, since inextensibility of the filament implies that the extension must vanish as $\alpha\to 0$ for fixed R. The terms which are subleading in R/L are precisely the terms which cause the deflection to vanish for small α, and they also lead to oscillations in δz as a function of α. Figures 3 and 4 show the dependence of f_t and f_r on α using formulas computed without assuming $R/L \ll 1$ (see the Appendix), for the case of $L/R=50$. Only the range from $\alpha=0$ to $\alpha=\pi/2$ is shown; f_t is even in α, and f_r is odd in α. A normal filament has $\alpha \approx 0.52$ rad $\approx 0.33\pi/2$ rad, which is in the region where the oscillations are relatively small.

B. Slender-body theory

Resistive-force theory fails to properly account for the long-range hydrodynamic interactions among the different elements of a slender body. The slender-body theory discussed in Sec. II accounts for these interactions, and gives a more accurate value for the external drag force per unit length **K**. Figure 5 shows **K** for a rotating helix with an open coil (the normal helix parameters given above), calculated by resistive-force theory and slender-body theory. The two calculations agree very well for the normal (K_1) component, with significant differences for the other two components. A much greater difference between the two theories is shown in Fig. 6, which displays the components of the drag forces per unit length for a close-coiled helix in axial flow. Each coil obstructs the flow to the next coil. Since slender-body theory accounts for this effect but resistive-force theory does not, the component of the force per unit length along the flow direction $\hat{\mathbf{z}}\cdot\mathbf{K} \approx \hat{\mathbf{b}}\cdot\mathbf{K}$ is substantially smaller in slender-body theory than in resistive-force theory.

Since the drag forces per unit length **K** must be computed numerically in slender-body theory, we numerically integrate to find the deflection of the end (see the Appendix). Our results are summarized in Table I. There is a fortuitous cancellation of errors leading to an accurate estimate for $\delta z(L)$ for a rotating normal helix. The resistive-force theory estimate is reasonably good for a normal helix subject to axial flow. However, the error made by resistive-force theory is large for a close-coiled helix.

C. Estimation of bending stiffness

We can use the results of the preceding subsections to make estimates for the bending stiffness of bacterial flagellar

TABLE I. The ratio of the extension computed by slender-body theory to the extension computed by resistive-force theory, $\delta z^{\mathrm{SBT}}(L)/\delta z^{\mathrm{RFT}}(L)$, for an open-coiled helix and a close-coiled helix.

Flow	Open coil	Close coil
axial	0.7869	0.2362
rotational	0.9917	0.3742

filaments. First consider the compression of a rotating helix due to viscous drag. Suppose that the body of the bacterium is held fixed (as when the cell is adhered to a glass cover slide), so that there is no external axial flow. The flagella of *E. coli* rotate at 100 Hz; it has been observed by Berg and collaborators that there is no noticeable difference in the axial length of rotating and de-energized flagella [36]. Thus, the change in axial length must be less than their experimental uncertainty of 0.2 μm. Taking the viscosity of water to be 10^{-3} N s/m^2, and using Eq. (11) for $\zeta_{\|}$, we find that the bending stiffness A for a normal filament must satisfy $A \geqslant 1.0 \times 10^{-24}$ N m^2. Using slender-body theory for this estimate leads to the same bound, $A \geqslant 1.0 \times 10^{-24}$ N m^2. Although our bound is consistent with the estimate of [19], $A \approx 10^{-24}$ N m^2, the more important implication of our calculation is that resistive-force theory is reasonably accurate for this geometry.

We can apply our calculation of the extension of a flexible helix in axial flow to the data of Hoshikawa and Kamiya, who used optical microscopy to record the deflection of a detached *S. typhimurium* filament in an external flow [24]. They used a bead and spring model to determine the bending stiffness. As mentioned in the Introduction, our model differs from theirs since we treat the filament as a continuum, and we use the slender-body theory to account for long-range hydrodynamic interactions. This last difference is crucial, since neglecting these interactions will lead to an overestimate of the bending stiffness. Although Hoshikawa and Kamiya observed large deflections, they found that the extension was linearly proportional to the speed of the external flow; the filament behaved like an ideal spring. Therefore, our small-deflection calculation should accurately capture the slope of the extension-velocity curve. Using their data from [24] and our resistive-force theory equations yields $A = 1.4 \times 10^{-23}$ N m^2; with the slender-body theory, the estimate is $A = 3.2 \times 10^{-24}$ N m^2.

D. Polarizable filament in an external field

An external electric field tends to align the tangent vector of a flagellar filament with the field direction. For example, straight polymorphic filaments align along the field, but close-coiled forms align with the helical axis perpendicular to the field [27]. The same effect will tend to unwind a flexible helical filament with a pitch intermediate between these two extremes. The helix will extend independent of its handedness, with the extension vanishing for $\alpha = 0$ (straight) and $\alpha = \pi/2$ (close-coiled). Following the approach outlined in the Appendix, we find

$$\frac{\delta z_f(L)}{L} = \frac{2R^2 \chi_a E^2}{A}\left[\cos\alpha - \frac{R}{L}\cot\alpha \sin\left(\frac{L\sin\alpha}{R}\right)\right]. \tag{30}$$

The graph of $\delta z_f(L)/L$ versus α is shown in Fig. 7. Washizu *et al.* report an induced dipole moment of 5×10^{-24} C m for a flagellar filament in a field of $E = 10^6$ V/m [27]. Since the filament is charged, the field oscillates at high frequency to keep the filament from moving. Assuming a filament of length 10 μm, this dipole moment corresponds to a susceptibility of $\chi_a \approx 5 \times 10^{-25}$ C m/V. For these values and $R = 0.2$ μm and $A \approx 10^{-24}$ N m^2, we expect a small deflection proportional to $R^2 \chi_a E^2 / A \approx 0.02$.

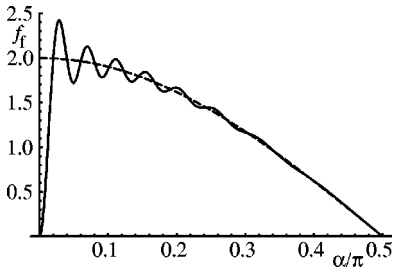

FIG. 7. Dimensionless extension f_f vs pitch angle α for a helix with four turns, $R = 0.22$ μm, and $P = 2.4$ μm, subject to an external field. The solid line is calculated using the exact expression for f_f, and the dotted line is $f_f = 2\cos\alpha$, the approximate dimensionless extension to leading order in R/L.

IV. CONCLUSION

In this article, we have calculated the deflection of helical filaments due to flow and external fields, placed a bound on the bending stiffness of *E. coli* flagellar filaments, and reinterpreted the data of Hoshikawa and Kamiya for *S. typhimurium* using slender-body hydrodynamics. These estimates could be refined by carrying out new experiments using fluorescent labeling of flagellar filaments [6] and subjecting them to various external loading conditions. For example, one end of a detached filament could be stuck to a magnetic bead turning rapidly enough to lead to a greater compression than that attained by a filament driven by *E. coli*'s flagellar motor. Likewise, one end of a detached fluorescent filament could be held in a uniform flow, as in the work of [24]. A third class of experiments would be to subject fluorescent filaments to an ac electric field, analogous to the dark-field experiments of [27]. In each of these three experimental situations, it has been shown that sufficiently great loading will lead to polymorphic transformations. Therefore, before generalizing the linear theory described here to handle large deflections, the next challenge is to incorporate polymorphism into the elastic theory.

Note added in proof. Recently, we became aware of the calculations of Flynn and Ma [37]. These authors find that C/A is approximately 22.7 for the filament. Such a ratio does not lead to qualitative changes in our results, but would lead to an order of magnitude estimate of C of approximately 10^{-24} N m^2 from our slender-body calculations and the data of [24].

ACKNOWLEDGMENTS

It is a pleasure to acknowledge useful conversations with H. Berg, K. Breuer, N. Darnton, G. Huber, S. Koehler, S. Rosjevskaya, J. Tang, and L. Turner. This work is supported in part by National Science Foundation Grant No. CMS-0093658 and the Defense Advanced Research Projects Agency BioMolecular Motors Program. T.R.P. thanks the As-

pen Center for Physics for hospitality while this work was being completed.

APPENDIX A: CALCULATION OF DEFORMATION

Consider a helical filament of length L with one end (at $s=0$) clamped and the other end (at $s=L$) free. We will study the steady-state deformation when the helix is subject to external loading. First we describe the general approach, then we consider the particular cases of end-loading, loading by flow, and loading by external field. We work to first order in the loading (the dimensionless parameters characterizing the magnitude of the loading are given below). Since the external force per unit length $\mathbf{K}$ vanishes when the load vanishes, $K_i=\hat{\mathbf{e}}_i\cdot\mathbf{K}\approx\hat{\mathbf{e}}_i^{(0)}\cdot\mathbf{K}$, where the errors are second order in the loading. A similar conclusion holds for N_i, F_i, and M_i. Thus, the components of the force balance equation, Eq. (7), to leading order are

$$\frac{dF_1}{ds}-\tau_0F_2+\kappa_0F_3+K_1=0, \tag{A1}$$

$$\frac{dF_2}{ds}+\tau_0F_1+K_2=0, \tag{A2}$$

$$\frac{dF_3}{ds}-\kappa_0F_1+K_3=0, \tag{A3}$$

where we have used Eq. (3) for the rate of change of the undeformed frame: $d\hat{\mathbf{e}}_i^{(0)}/ds=\mathbf{\Omega}^{(0)}\times\hat{\mathbf{e}}_i^{(0)}$. Since the end at $s=L$ is free, the boundary conditions for these equations are $F_i(L)=0$ for the cases of loading by drag and external field.

Equations of the same form as Eqs. (A1)–(A3) appear several places in our analysis. The general solution is given by

$$F_1=C_0\sin(\sigma s)+\sin(\sigma s)/\sigma\int ds'\cos(\sigma s')P - \cos(\sigma s)/\sigma\int ds'\sin(\sigma s')P, \tag{A4}$$

$$F_2=\int ds'(K_2-\tau_0F_1), \tag{A5}$$

$$F_3=\int ds'(K_3+\kappa_0F_1), \tag{A6}$$

where $\sigma=\sqrt{\kappa_0^2+\tau_0^2}=\sin(\alpha)/R$, $P=(\tau_0K_2-\kappa_0K_3+dK_1/ds)$, and the integration constant C_0 is determined by substituting the expressions for the F_i from Eqs. (A4)–(A6) into Eq. (A1).

The components of the moment balance equation, Eq. (8), to leading order are

$$\frac{dM_1}{ds}-\tau_0M_2+\kappa_0M_3-F_2+N_1=0, \tag{A7}$$

$$\frac{dM_2}{ds}+\tau_0M_1+F_1+N_2=0, \tag{A8}$$

$$\frac{dM_3}{ds}-\kappa_0M_1+N_3=0 \tag{A9}$$

with $M_i(L)=0$ for the cases of loading by drag and external field.

Once the moment is found by formulas analogous to Eqs. (A4)–(A6), the strain vector $\mathbf{\Omega}$ is determined by the constitutive relation, Eq. (6). Let $\delta\mathbf{\Omega}\equiv\mathbf{\Omega}-\mathbf{\Omega}^{(0)}$; then, since we assume $C=A$,

$$\delta\Omega_i\equiv\hat{\mathbf{e}}_i\cdot\delta\mathbf{\Omega}=\hat{\mathbf{e}}_i^{(0)}\cdot\delta\mathbf{\Omega}=M_i/A. \tag{A10}$$

The next step is to integrate Eq. (3) to find $\hat{\mathbf{e}}_i=\hat{\mathbf{e}}_i^{(0)}+\delta\hat{\mathbf{e}}_i$; to first order, Eq. (3) is

$$\frac{d(\delta\hat{\mathbf{e}}_i)}{ds}=\mathbf{\Omega}^{(0)}\times\delta\hat{\mathbf{e}}_i+\delta\mathbf{\Omega}\times\hat{\mathbf{e}}^{(0)}. \tag{A11}$$

Solving Eq. (A11) amounts to finding the rotation which carries the frame $\hat{\mathbf{e}}_i^{(0)}(s)$ to the frame $\hat{\mathbf{e}}_i(s)$. Since the deformation is small, this rotation is close to the identity, and

$$\delta\hat{\mathbf{e}}_i=J_{ij}\hat{\mathbf{e}}_j^{(0)}, \tag{A12}$$

where J_{ij} is an antisymmetric matrix [note that Eq. (A12) properly ensures that $\delta\hat{\mathbf{e}}_i\cdot\hat{\mathbf{e}}_i^{(0)}=0$]. In terms of J_{ij}, Eq. (A11) is

$$\frac{dJ_{ij}}{ds}=\epsilon_{ijk}(\delta\Omega_k+\Omega_l^{(0)}J_{lk}), \tag{A13}$$

where ϵ_{ijk} is the totally antisymmetric symbol. If $J_i=\epsilon_{ijk}J_{jk}$, then Eq. (A13) becomes

$$\frac{dJ_1}{ds}-\tau_0J_2+\kappa_0J_3=\delta\Omega_1, \tag{A14}$$

$$\frac{dJ_2}{ds}+\tau_0J_1=\delta\Omega_2, \tag{A15}$$

$$\frac{dJ_3}{ds}-\kappa_0J_1=\delta\Omega_3. \tag{A16}$$

We assume clamped boundary conditions at $s=0$, so that $\hat{\mathbf{e}}_i(0)=\hat{\mathbf{e}}_i^{(0)}(0)$, or $J_i(0)=0$. Once Eqs. (A14)–(A16) are solved, the tangent vector is given by

$$\hat{\mathbf{e}}_3=\hat{\mathbf{e}}_3^{(0)}+J_2\hat{\mathbf{e}}_1^{(0)}-J_1\hat{\mathbf{e}}_2^{(0)}. \tag{A17}$$

Finally, to find the z component of the deflection of the free end, we integrate,

$$\delta z(L)=\int_0^L ds'\hat{\mathbf{z}}\cdot\delta\hat{\mathbf{e}}_3=-\int_0^L ds'J_1\sin\alpha. \tag{A18}$$

The choice of lower limit in the integral of Eq. (A18) enforces the boundary condition $z(0)=0$.

We now apply these equations to the particular cases discussed in the body of this article.

1. End-loading

This case is classical and is included only for comparison. One end of the rod is subject to $\mathbf{F}=F\hat{\mathbf{z}}$. Since there is no

external force per unit length, the force acting on each cross section of the rod is constant: $\mathbf{F}(s)=F\hat{\mathbf{z}}$. We work to first order in FR^2/A. As discussed in the text, there are two cases, depending on the line of action of $\mathbf{F}$. Consider first the case in which the line of action of $\mathbf{F}$ is the axis of the helix. Then the force contributes a moment about the origin of the rod, $\mathbf{r}(0)=\mathbf{0}$. Solving the moment equations, Eqs. (A7)–(A9), with the constant force and $N_i=0$ leads to $M_1=-FR\cos\alpha$, $M_2=FR\sin\alpha$, and $M_3=0$. Using these moments to compute $\delta\hat{\mathbf{e}}_3$ and $\delta z(L)$ leads to Eq. (23).

If the line of action of $\mathbf{F}$ is parallel to the z axis but passing through the origin, then there will be no moment at $s=L$. This change in the boundary conditions leads to moments that depend on s,

$$M_1 = RF\cos\alpha\sin[\sigma(s-L)], \tag{A19}$$

$$M_2 = RF(\tau_0/\sigma)\cos\alpha\{\cos[\sigma(s-L)]-1\}, \tag{A20}$$

$$M_3 = RF(\kappa_0/\sigma)\{1-\cos[\sigma(s-L)]\}. \tag{A21}$$

Integrating these moments using our general approach to find $\delta z(L)$ leads to Eq. (24).

2. Loading by hydrodynamic drag

In this case we work to first order in $\eta v LR^2/A$. In resistive-force theory, the force per unit length acting on the rod is uniform for axial flow,

$$K_1^{\mathrm{t}} = 0, \tag{A22}$$

$$K_2^{\mathrm{t}} = 2\zeta_{\parallel} v\sin\alpha, \tag{A23}$$

$$K_3^{\mathrm{t}} = \zeta_{\parallel}\cos\alpha, \tag{A24}$$

and also for rotational flow,

$$K_1^{\mathrm{r}} = 0, \tag{A25}$$

$$K_2^{\mathrm{r}} = 2\zeta_{\parallel} v\cos\alpha, \tag{A26}$$

$$K_3^{\mathrm{r}} = -\zeta_{\parallel} v\sin\alpha, \tag{A27}$$

where $v=\omega R$ in Eqs. (A25)–(A27).

The force per unit length for a helix hanging under its own weight (or a charged helix in a dc electric field) is also uniform, and easily handled by our method. Thus, we also consider a helix to an isotropic force per unit length $\mathbf{K}=w\hat{\mathbf{z}}$,

$$K_1^{\mathrm{w}} = 0, \tag{A28}$$

$$K_2^{\mathrm{w}} = w\sin\alpha, \tag{A29}$$

$$K_3^{\mathrm{w}} = w\cos\alpha. \tag{A30}$$

Solving Eqs. (A1)–(A3) for uniform K_i, we find

$$F_1 = \frac{K_{\varphi}}{\sigma}\{1-\cos[\sigma(L-s)]\}, \tag{A31}$$

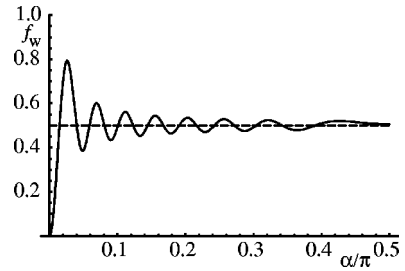

FIG. 8. Dimensionless extension f_{w} vs pitch angle α for a helix with four turns, $R=0.22$ μm, and $P=2.4$ μm, subject to external force per unit length $\mathbf{K}=w\hat{\mathbf{z}}$. The solid line is calculated using the exact expression for f_{w}, and the dotted line is $f_{\mathrm{w}}=1/2$, the approximate dimensionless extension to leading order in R/L.

$$F_2 = \frac{K_z\kappa_0}{\sigma}(L-s) - \frac{K_{\varphi}\tau_0}{\sigma^2}\sin[\sigma(L-s)], \tag{A32}$$

$$F_3 = \frac{K_z\tau_0}{\sigma}(L-s) + \frac{K_{\varphi}\kappa_0}{\sigma^2}\sin[\sigma(L-s)], \tag{A33}$$

where $K_{\varphi}=-K_2\cos\alpha+K_3\sin\alpha$ and $K_z=K_2\sin\alpha+K_3\cos\alpha$. Note that σ is the periodicity of the helix measured along its arc length. Integrating the moment equations, Eqs. (A7) and (A8), with these forces results in

$$M_1 = -(\tau_0K_{\varphi}+\kappa_0K_z)\{1-\cos[\sigma(L-s)]\}/\sigma^3 + \tau_0K_{\varphi}(L-s)\sin[\sigma(L-s)]/\sigma^2, \tag{A34}$$

$$M_2 = \kappa_0(\kappa_0K_{\varphi}-\tau_0K_z)(L-s)/\sigma^3 + [\kappa_0\tau_0K_z + (\tau_0^2-\kappa_0^2)K_{\varphi}]\sin[\sigma(L-s)]/\sigma^4 - \tau_0^2K_{\varphi}(L-s)\cos[\sigma(L-s)]/\sigma^3, \tag{A35}$$

$$M_3 = \kappa_0(\tau_0K_{\varphi}+\kappa_0K_z)(L-s)/\sigma^3 - (2\kappa_0\tau_0K_{\varphi}+\kappa_0^2K_z)\sin[\sigma(L-s)]/\sigma^4 + \kappa_0\tau_0K_{\varphi}(L-s)\cos[\sigma(L-s)]/\sigma^3. \tag{A36}$$

For the case of viscous drag, these moments lead to the extensions of Eqs. (28) and (29), shown in Figs. 3 and 4. For an isotropic external force per unit length, Eqs. (A28)–(A30), the extension to leading order in R/L is

$$\frac{\delta z_{\mathrm{w}}(L)}{L} = \frac{wR^2L}{2A}f_{\mathrm{w}}(\alpha,R/L). \tag{A37}$$

Figure 8 shows the extension to all orders in R/L for a helix with four turns and the pitch and radius of a normal flagellar filament.

For the slender-body calculation of the deformation of a helix in axial or rotational flow, we use Eq. (19) to solve $\mathbf{K}$, and then numerically integrate to eventually find $\delta z(L)$.

3. Loading by external field

In this case, the external force per unit length vanishes, implying $\mathbf{F}=\mathbf{0}$. But the field exerts a moment per unit length on the filament; for $\mathbf{E}=E\hat{\mathbf{z}}$, the only nonvanishing component of $\mathbf{N}$ is $N_1=\chi_{\mathrm{a}}E^2R\cos\alpha\sin\alpha$ [see Eq. (22)]. Here the small

parameter is $\chi_a E^2 R^2/A$. Solving Eqs. (A7)–(A9) for this case leads to

$$M_1 = R\chi_a E^2 \cos\alpha \sin[\sigma(s-L)], \tag{A38}$$

$$M_2 = R\chi_a E^2 (\tau_0/\sigma)\cos\alpha\{\cos[\sigma(s-L)]-1\}, \tag{A39}$$

$$M_3 = R\chi_a E^2 (\kappa_0/\sigma)\{1-\cos[\sigma(s-L)]\}. \tag{A40}$$

Note that this moment has the same functional form as the moment for end-loading, Eqs. (A19)–(A21), which explains why the extension due to an external field, Eq. (30), has the same dependence on L as in Eq. (24).

[1] D. Bray, *Cell Movements: From Molecules to Motility*, 2nd ed. (Garland Publishing, Inc., New York, 2001).
[2] E. M. Purcell, Am. J. Phys. **45**, 3 (1977).
[3] H. C. Berg, *E. coli in Motion* (Springer-Verlag, New York, 2004).
[4] R. M. Macnab and M. K. Ornston, J. Mol. Biol. **112**, 1 (1977).
[5] M. J. Kim, J. C. Bird, A. J. Van Parys, K. S. Breuer, and T. R. Powers, Proc. Natl. Acad. Sci. U.S.A. **100**, 15 481 (2003).
[6] L. Turner, W. S. Ryu, and H. C. Berg, J. Bacteriol. **182**, 2793 (2000).
[7] J. L. L. Higdon, J. Fluid Mech. **90**, 685 (1979).
[8] J. Lighthill, J. Eng. Math. **30**, 35 (1996).
[9] M. Ramia, D. L. Tullock, and N. Phan-Thien, Biophys. J. **65**, 755 (1993).
[10] M. J. Kim and T. R. Powers, Phys. Rev. E **69**, 061910 (2004).
[11] J. Lighthill, SIAM Rev. **18**, 161 (1975).
[12] J. Rotne and S. Prager, J. Chem. Phys. **50**, 4831 (1969).
[13] K. E. Machin, J. Exp. Biol. **35**, 796 (1958).
[14] C. H. Wiggins and R. E. Goldstein, Phys. Rev. Lett. **80**, 3879 (1998).
[15] T. R. Powers, Phys. Rev. E **65**, 040903(R) (2002).
[16] S. A. Koehler and T. R. Powers, Phys. Rev. Lett. **85**, 4827 (2000).
[17] R. E. Goldstein, A. Goriely, G. Huber, and C. W. Wolgemuth, Phys. Rev. Lett. **84**, 1631 (2000).
[18] Y. Takano and T. Goto, JSME Int. J., Ser. C **46**, 1234 (2003).
[19] Y. Takano, K. Yoshida, S. Kudo, M. Nishitoba, and Y. Magariyama, JSME Int. J., Ser. C **46**, 1241 (2003).
[20] J. Gray and G. J. Hancock, J. Exp. Biol. **32**, 802 (1955).
[21] R. E. Johnson and C. J. Brokaw, Biophys. J. **25**, 113 (1979).
[22] H. Flores, E. Lobaton, S. Méndez-Diez, S. Tlupova, and R. Cortez, Bull. Math. Biol. (to be published).
[23] S. Fujime, M. Maruyama, and S. Asakura, J. Mol. Biol. **68**, 347 (1972).
[24] H. Hoshikawa and R. Kamiya, Biophys. Chem. **22**, 159 (1985).
[25] L. D. Landau and E. M. Lifshitz, *Theory of Elasticity*, 3rd ed. (Pergamon Press, Oxford, 1986).
[26] S. Trachtenberg and I. Hammel, J. Struct. Biol. **109**, 18 (1992).
[27] M. Washizu, M. Shikida, S. Aizawa, and H. Hotani, IEEE Trans. Ind. Appl. **28**, 1194 (1992).
[28] G. Maret and K. Dransfeld, in *Strong and Ultrastrong Magnetic Fields and their Applications*, Vol. 57 of *Topics in Applied Physics*, edited by F. Herlach (Springer-Verlag, New York, 1985).
[29] R. D. Kamien, Rev. Mod. Phys. **74**, 953 (2002).
[30] R. L. Bishop, Am. Math. Monthly **82**, 246 (1975).
[31] R. E. Goldstein, T. R. Powers, and Chris H. Wiggins, Phys. Rev. Lett. **80**, 5232 (1998).
[32] C. W. Wolgemuth, R. E. Goldstein, and T. R. Powers, Physica D **190**, 266 (2004).
[33] J. B. Keller and S. I. Rubinow, J. Fluid Mech. **75**, 705 (1976).
[34] C. J. Brokaw, J. Exp. Biol. **53**, 445 (1970).
[35] A. E. H. Love, *A Treatise on the Mathematical Theory of Elasticity*, 4th ed. (Dover Publications, New York, 1944).
[36] H. C. Berg, N. Darnton, S. Rojevskaya, and L. Turner (private communication).
[37] T. C. Flynn and J. Ma, Biophys. J. **86**, 3204 (2004).